

Singular Asymptotics of SPADE in Quantum Source Discrimination

Natsuki Kariya^{1,*}

¹*Mizuho Bank, Informatics and Mathematics Research Institute,
1-5-5 Otemachi, Chiyoda-ku, Tokyo 100-8176, Japan*

(Dated: May 15, 2026)

We study far-field discrimination between one and two incoherent point sources in the singular regime of weak and closely spaced emitters. Under ideal alignment, spatial-mode demultiplexing (SPADE) attains the quantum-optimal large-sample Stein exponent, but the finite-photon behavior near the one-source boundary and the effect of realistic imperfections remain less understood. Using singular learning theory, we analyze both the aligned and misaligned problems. In the aligned Gaussian case, we derive the zeta-function poles for direct imaging and SPADE, show that both share the same real log canonical threshold $\lambda = 1/2$ but differ in multiplicity, and obtain the corresponding Bayes free-energy asymptotics. This yields a universal subleading advantage of aligned SPADE in the local prior-weighted regime. In the misaligned setting, we study a physically motivated binary-SPADE reduction that retains the full leading $O(s^2)$ leakage contrast near alignment, with corrections from the detailed higher-mode redistribution entering only at $O(s^4)$. We show that misaligned binary-SPADE and direct imaging acquire nontrivial local power on different intrinsic scales, $s = O(n^{-1/4})$ and $s = O(n^{-1/2})$, respectively. However, finite- n Neyman–Pearson comparisons under common physical conditions reveal that direct imaging is stronger on the plotted grids and that misaligned binary-SPADE exhibits an exact blind separation $s^* = 2\theta$, where its power collapses to α . These results identify model singularity as a structural organizing principle for finite-photon quantum discrimination and clarify how ideal aligned SPADE benchmarks can fail to translate into finite- n advantages under misalignment.

I. INTRODUCTION

Determining whether observed light originates from one incoherent point source or from two is a minimal but fundamental problem in optical detection. Despite its apparent simplicity, it already captures the essential difficulty of resolving faint and closely spaced emitters, a situation that arises naturally in microscopy and observational astronomy. The problem is especially challenging in the practically important regime where the source separation is very small or one source is much weaker than the other.

The Rayleigh criterion has traditionally been regarded as the classical resolution limit for resolving two closely spaced incoherent sources by direct imaging. More recently, however, spatial-mode demultiplexing (SPADE) was proposed as a quantum-measurement-inspired detection scheme and shown to surpass the Rayleigh limit and, under ideal conditions, to attain the quantum-optimal limit for source discrimination and separation [1–3].

Experimental demonstrations and analyses of more realistic settings soon followed, including studies of source asymmetry, misalignment, and imperfect demultiplexing [4, 6, 7]. In particular, Schlichtholz et al. [15] showed that quantum-optimal tests for aligned SPADE lose all discrimination power under arbitrarily small misalignment of the demultiplexer, thereby sharply illustrating how fragile the ideal aligned benchmark can be and motivating the search for robust alternatives. These results establish the ideal large-sample benchmark clearly,

but they also leave two further questions: how finite-photon behavior is modified near the one-source boundary, and what structural mechanism causes the ideal aligned benchmark to fail to translate into a practical advantage under misalignment. In the present paper we address both questions through the lens of singular learning theory.

The difficulty of source discrimination in these regimes has a precise statistical origin. When the two sources are extremely close, or when the secondary source is extremely weak, different parameter values of the two-source model can generate the same observable probability distribution, including the distribution of the one-source null model. The parameterization then ceases to distinguish observable distributions one by one. Equivalently, the map from model parameters to probability distributions is no longer one-to-one, and the Fisher information matrix becomes singular. In statistics, such models lie outside the standard regular framework; consequently, familiar results such as Fisher-information-based asymptotics and the standard χ^2 asymptotics for likelihood-ratio tests need not hold [8, 9]. Although singular models are ubiquitous in modern statistics, a general framework for their analysis—singular learning theory—has emerged from Bayesian statistics only relatively recently and is still evolving [10–12]. The present one-versus-two-source discrimination problem is a natural setting in which these ideas become physically relevant, because the one-source model sits precisely on a singular boundary of the two-source family.

Among realistic imperfections, detector misalignment is especially natural from both the experimental and theoretical viewpoints. Experimentally, it directly af-

* natsuki.kariya@mizuho-rt.co.jp

fects discrimination performance. Theoretically, it removes the exact support mismatch of ideally aligned SPADE without obscuring the measurement model with additional complications, so the one-source versus two-source comparison can be formulated through an ordinary likelihood-ratio analysis with nontrivial null fluctuations. At the same time, near alignment the dominant local effect of a small displacement is still the leakage of probability out of the lowest-order SPADE mode. For a Gaussian point-spread function, this leakage is $O(s^2)$, whereas the total redistribution into modes $q \geq 2$ is only $O(s^4)$. Thus the binary statistic $q = 0$ versus $q \geq 1$ retains the full leading local contrast relevant to the near-alignment regime, while yielding the simplest nontrivial singular testing problem induced by misalignment.

In this paper, we develop a singular-learning-theoretic analysis of far-field one-versus-two-source discrimination, with particular emphasis on the relation between structural local asymptotics and finite- n performance under common physical conditions. In the aligned Gaussian case, we derive the zeta-function structure for direct imaging and aligned SPADE and show that the two schemes share the same real log canonical threshold $\lambda = 1/2$ but differ in multiplicity. As a result, they have the same leading $\frac{1}{2} \log n$ growth of the Bayes free energy, while direct imaging carries an additional $-\log \log n$ correction. We also provide a numerical validation across several bounded prior windows in the weak-companion, sub-Rayleigh regime, showing that the centered finite- n Bayes free energy is already well described, in the central part of its distribution, by the singular local model.

We then turn to the misaligned setting and study a physically motivated misaligned binary-SPADE model. There we derive the local likelihood-ratio statistics and show that direct imaging and misaligned binary-SPADE acquire nontrivial local power on different intrinsic scales, $s = O(n^{-1/2})$ and $s = O(n^{-1/4})$, respectively. This intrinsic-scale statement is structural: it identifies the local windows in which each scheme first develops nontrivial power near the singular boundary. It does not by itself determine which scheme performs better at a common physical separation, brightness ratio, detector offset, and sample size. To make that bridge explicit, we therefore supplement the local asymptotic analysis with finite- n Neyman–Pearson comparisons under common physical conditions. For the representative regime considered here, direct imaging is consistently stronger on the plotted grids, while the misaligned binary-SPADE model exhibits an exact blind separation $s^* = 2\theta$, at which its coarse-grained alternative becomes identical to the null and its power collapses to the significance level. In this sense, the ideal aligned large-sample SPADE benchmark does not directly translate into a finite- n advantage for the misaligned binary-SPADE model studied here.

These results identify model singularity as a structural feature of finite-photon quantum discrimination rather than a merely technical complication. More broadly, they show that the usual large-sample ordering of mea-

surement schemes can become qualitatively misleading near singular boundaries and under realistic imperfections. Extending this viewpoint to other imperfections, other measurements, and broader quantum hypothesis-testing settings remains an important direction for future work.

II. PROBLEM SETUP AND LARGE-SAMPLE BENCHMARKS

We briefly recall the large- n benchmarks for one-versus-two-source discrimination that will be needed below, following Ref. [5], and fix notation. We consider a one-dimensional diffraction-limited imaging system with normalized point-spread function (PSF) $\psi(x)$ satisfying $\int dx |\psi(x)|^2 = 1$. Since the absolute source position is irrelevant for the present discussion, we place the bright source at the origin. The null hypothesis H_0 corresponds to a single incoherent source, whereas under the alternative hypothesis H_1 a second incoherent source of relative brightness $\epsilon \ll 1$ is present at separation s :

$$p_0(x) = |\psi(x)|^2, \quad (1)$$

$$p_1(x) = (1 - \epsilon)|\psi(x)|^2 + \epsilon|\psi(x - s)|^2. \quad (2)$$

We focus on the sub-Rayleigh weak-companion regime, $\epsilon \ll 1$ and $|s|$ smaller than the width of the PSF. In direct imaging, each detection event returns a position X_i on the one-dimensional image plane, so that after n detections one obtains independent samples $X^n = (X_1, \dots, X_n)$ from either p_0 or p_1 . For a fixed type-I error tolerance $0 < \alpha < 1$, let $\beta_n^{\text{DI}}(\alpha)$ denote the minimum type-II error achievable by direct imaging after n detected photons. Classical Stein’s lemma gives

$$-\lim_{n \rightarrow \infty} \frac{1}{n} \log \beta_n^{\text{DI}}(\alpha) = D(p_0 \| p_1), \quad (3)$$

where

$$D(p_0 \| p_1) := \int dx p_0(x) \log \frac{p_0(x)}{p_1(x)}.$$

For a Gaussian PSF,

$$\psi(x) = \left(\frac{1}{2\pi\sigma^2} \right)^{1/4} \exp\left(-\frac{x^2}{4\sigma^2} \right),$$

the weak-companion expansion yields

$$D(p_0 \| p_1) = \frac{\epsilon^2 s^2}{2\sigma^2} + O(\epsilon^2 s^4, \epsilon^3). \quad (4)$$

Thus, for direct imaging, the Stein exponent vanishes as $\epsilon^2 s^2$ in the limit of a faint and nearby secondary source.

A quantum description associates to a single detected photon the states

$$|\psi_x\rangle := \int dx' \psi(x' - x) a^\dagger(x')|0\rangle,$$

so that

$$\rho_0 = |\psi_0\rangle\langle\psi_0|, \quad (5)$$

$$\rho_1 = (1 - \epsilon)|\psi_0\rangle\langle\psi_0| + \epsilon|\psi_s\rangle\langle\psi_s|. \quad (6)$$

Let $\beta_n^Q(\alpha)$ denote the minimum type-II error optimized over all quantum measurements. Quantum Stein's lemma then implies

$$-\lim_{n \rightarrow \infty} \frac{1}{n} \log \beta_n^Q(\alpha) = D(\rho_0 \| \rho_1), \quad (7)$$

where

$$D(\rho \| \sigma) := \text{Tr}[\rho(\log \rho - \log \sigma)].$$

For the rank-two model in Eq. (6), one has

$$D(\rho_0 \| \rho_1) = (1 - |\langle\psi_0|\psi_s\rangle|^2)\epsilon + O(\epsilon^2).$$

For the Gaussian PSF, this becomes

$$D(\rho_0 \| \rho_1) = \frac{\epsilon s^2}{4\sigma^2} + O(\epsilon s^4, \epsilon^2). \quad (8)$$

The quantum benchmark therefore improves the scaling of the error exponent from $\epsilon^2 s^2$ to ϵs^2 .

A concrete measurement that attains this quantum benchmark, under ideal alignment, is spatial-mode demultiplexing (SPADE) [1, 5]. In SPADE, one does not record the continuous image-plane position of each detected photon. Instead, one projects the optical field onto an orthonormal Hermite–Gaussian mode basis $\{|\phi_q\rangle\}_{q=0}^\infty$ adapted to the Gaussian PSF, and records the detected mode label q . The corresponding outcome distributions under the null and alternative hypotheses are therefore

$$P_0(q) = \text{Tr}(\Pi_q \rho_0) = |\langle\phi_q|\psi_0\rangle|^2, \quad (9)$$

$$\begin{aligned} P_1(q) &= \text{Tr}(\Pi_q \rho_1) \\ &= (1 - \epsilon)|\langle\phi_q|\psi_0\rangle|^2 + \epsilon|\langle\phi_q|\psi_s\rangle|^2, \end{aligned} \quad (10)$$

where $\Pi_q := |\phi_q\rangle\langle\phi_q|$. Once the measurement is fixed, SPADE reduces the quantum discrimination problem to an ordinary classical hypothesis test for the discrete outcome distribution $\{P_a(q)\}_{q \geq 0}$. In the perfectly aligned Gaussian setting, the resulting Kullback–Leibler information coincides, to leading order, with the quantum benchmark in Eq. (8). The results recalled in this section concern the ideal large-sample regime in which (ϵ, s) are fixed as $n \rightarrow \infty$. They provide the standard reference point for comparing direct imaging, the quantum optimum, and aligned SPADE. However, they do not describe the finite-photon corrections or the singular local regimes in which ϵ and/or s approach the one-source boundary as n increases. Those are the regimes addressed in the following sections.

III. TESTING QUANTITIES, BAYES FACTORS, AND SINGULAR ASYMPTOTIC REGIMES

To analyze the finite-photon behavior of source discrimination, we formulate the problem within a Bayesian hypothesis-testing framework that covers both direct imaging and SPADE. The data consist of n independent measurement outcomes

$$Y^n = (Y_1, \dots, Y_n),$$

obtained from a fixed measurement. For direct imaging, $Y_i = X_i \in \mathbb{R}$ denotes the detected image-plane coordinate, whereas for SPADE, $Y_i = q_i \in \{0, 1, 2, \dots\}$ denotes the detected Hermite–Gaussian mode label.

Throughout this paper, the null hypothesis H_0 is the one-source model introduced in Sec. II, while the alternative hypothesis H_1 is the two-source model parameterized by

$$w \in W,$$

where w collects the relevant parameters, such as the relative brightness ϵ , the source separation s . We equip H_1 with a prior density $\phi(w)$ on W . In the misaligned analysis below, the detector offset θ is treated as a fixed external parameter rather than as a parameter endowed with a prior, since our interest is in the local behavior with respect to (ϵ, s) at a given misalignment. Let $p_0(y)$ denote the distribution of a single measurement outcome under H_0 , and let $p(y|w)$ denote the corresponding distribution under H_1 . For direct imaging, these are the image-plane densities in Eqs. (1) and (2); for SPADE, they are the mode-resolved probabilities in Eqs. (9) and (10). The corresponding marginal likelihoods are

$$m_0(Y^n) = \prod_{i=1}^n p_0(Y_i), \quad (11)$$

$$m_1(Y^n) = \int_W \prod_{i=1}^n p(Y_i|w) \phi(w) dw. \quad (12)$$

It is useful to distinguish two levels of testing quantities.

First, in the large-sample benchmarks of Sec. II, the type-II errors

$$\beta_n^\mu(\alpha), \quad \mu \in \{\text{DI}, Q, \text{SPADE}\},$$

refer to ordinary fixed-significance Neyman–Pearson testing at fixed model parameters, such as fixed (ϵ, s) .

Second, once the composite alternative is equipped with the prior ϕ , it induces the Bayes-averaged alternative law m_1 in Eq. (12). The comparison between m_0 and m_1 is then an ordinary simple-versus-simple testing problem, and its natural likelihood-ratio statistic is the Bayes factor

$$\Lambda_n(Y^n) := \frac{m_1(Y^n)}{m_0(Y^n)}. \quad (13)$$

By the Neyman–Pearson lemma, for a prescribed type-I error tolerance α , the most powerful test for m_0 versus m_1 rejects H_0 for sufficiently large Λ_n .

Equivalently, one may use

$$F_n(Y^n) := -\log \Lambda_n(Y^n) \quad (14)$$

as the test statistic, so that the rejection region is defined by $F_n \leq \eta$ for an appropriate threshold η . It is also convenient to introduce the partial free energies

$$F_{0,n}(Y^n) := -\log m_0(Y^n), \quad F_{1,n}(Y^n) := -\log m_1(Y^n), \quad (15)$$

for which

$$F_n(Y^n) = F_{1,n}(Y^n) - F_{0,n}(Y^n). \quad (16)$$

Thus the log Bayes factor is the difference of two free energies in the usual singular-learning-theoretic sense.

The central issue is that, in the source-discrimination problem, the null model is realized at a singular point of the alternative model. Indeed, when the source separation vanishes, or when the secondary-source intensity vanishes, multiple points—and in general higher-dimensional subsets—of the parameter space W yield the same observable distribution $p_0(y)$. To characterize this structure, let

$$K(w) := \int p_0(y) \log \frac{p_0(y)}{p(y|w)} d\nu(y) \quad (17)$$

be the Kullback–Leibler function of the alternative model relative to H_0 , and define the associated zeta function

$$\zeta(z) := \int_W K(w)^z \phi(w) dw. \quad (18)$$

Here $d\nu(y)$ denotes the underlying measure on the outcome space: it is the Lebesgue measure for direct imaging and the counting measure for SPADE.

In singular learning theory, the asymptotic behavior of the marginal likelihood is governed by the largest pole of $\zeta(z)$ (the minimal review of singular learning theory is given in Appendix D). Denoting by λ the real log canonical threshold and by m its multiplicity, one obtains the singular asymptotic expansion

$$-\log m_1(Y^n) = -\sum_{i=1}^n \log p_0(Y_i) + \lambda \log n \quad (19)$$

$$- (m-1) \log \log n + O_p(1), \quad (20)$$

where the $O_p(1)$ term remains random in the large- n limit. Accordingly, the log Bayes factor, or equivalently the free-energy difference, takes the form

$$F_n(Y^n) = \lambda \log n - (m-1) \log \log n + O_p(1). \quad (21)$$

It is useful to remark on the relation to the usual KL/Stein regime. The singular expansion in Eq. (21) is the boundary case relevant to the present source-discrimination problem, in which the null distribution is realized at a singular point of the alternative model and hence

$$K_* := \inf_{w \in W} K(w) = 0.$$

More generally, if the null distribution is not exactly realized within the alternative model, then the leading term of the marginal likelihood is governed by the positive minimum

$$K_* = \inf_{w \in W} K(w) > 0,$$

and one expects

$$F_n(Y^n) = nK_* + \lambda \log n - (m-1) \log \log n + O_p(1).$$

In that case, the normalized log Bayes factor satisfies

$$\frac{1}{n} F_n(Y^n) \rightarrow K_*(n \rightarrow \infty),$$

so the leading behavior is controlled by the minimum Kullback–Leibler information, in direct analogy with the usual large-sample error exponent in Stein-type asymptotics. The present singular regime corresponds to the special boundary situation $K_* = 0$, where the $O(\log n)$ terms become leading and reveal the higher-order structure invisible in the ordinary regular picture.

We also comment on the relation between our analysis and the existing analysis of aligned-SPADE. In the ideal aligned-SPADE setting, the null outcome distribution is concentrated entirely on the lowest-order mode: under H_0 , every detected photon falls in $q = 0$. As a result, the usual null-side likelihood-ratio statistic has no nontrivial fluctuations, so the standard fixed-significance Neyman–Pearson interpretation is not the natural one in this case. The aligned-SPADE asymptotics derived below should therefore be understood as statements about the singular Bayes free energy and the corresponding prior-weighted local behavior obtained after integrating over nearby composite alternatives, rather than about an ordinary fixed- α type-II error at a fixed alternative parameter. To keep this distinction explicit, we denote the corresponding local Bayes-integrated quantity by

$$\bar{\beta}_{n,\phi}^{\mu,\text{loc}},$$

where μ labels the measurement scheme.

This distinction is crucial in the present problem. In regular models, the leading deterministic term often suffices to characterize the asymptotic behavior of a test statistic. In singular models, however, both the deterministic logarithmic terms and the stochastic $O_p(1)$ contribution matter. It is precisely this singular asymptotic structure that we analyze below for the aligned and misaligned source-discrimination problems.

IV. MAIN RESULTS

We now present the main consequences of the singular-learning-theoretic framework for far-field one-versus-two-source discrimination. Our analysis addresses two complementary questions. First, in the perfectly aligned setting, where SPADE attains the quantum-optimal Stein exponent in the ideal large-sample limit, we ask how model singularity modifies the corresponding local Bayes-integrated behavior in the finite-photon regime. Second, in the misaligned setting, the exact support mismatch of ideal alignment is removed, and one is naturally led to a likelihood-ratio-based local analysis. There we compare direct imaging with the misaligned binary-SPADE model, whose local power becomes nontrivial on an intrinsic scale different from that of direct imaging.

A. Aligned case: singular corrections to Bayes-integrated local behavior

We first reconsider the perfectly aligned setting from the viewpoint of singular learning theory. To make contact with Sec. II, we use the same parameters ϵ and s throughout. The singular point corresponding to the one-source model is then located at

$$(\epsilon, s) = (0, 0).$$

For direct imaging, the relevant Kullback–Leibler information is precisely the divergence introduced in Sec. II:

$$D_{\text{DI}}(\epsilon, s) := D(p_0 \| p_1). \quad (22)$$

For the Gaussian PSF, Eq. (4) gives

$$D_{\text{DI}}(\epsilon, s) = \frac{\epsilon^2 s^2}{2\sigma^2} + O(\epsilon^2 s^4, \epsilon^3). \quad (23)$$

For aligned SPADE, the relevant information is the Kullback–Leibler divergence between the mode-resolved outcome distributions:

$$D_{\text{SPADE}}(\epsilon, s) := \sum_{q=0}^{\infty} P_0(q) \log \frac{P_0(q)}{P_1(q)}. \quad (24)$$

In the perfectly aligned Gaussian setting, this measurement attains the quantum Stein benchmark, so that its leading term agrees with that of $D(\rho_0 \| \rho_1)$:

$$D_{\text{SPADE}}(\epsilon, s) = D(\rho_0 \| \rho_1) + O(\epsilon^2) = \frac{\epsilon s^2}{4\sigma^2} + O(\epsilon s^4, \epsilon^2). \quad (25)$$

Thus, at the level of the leading Kullback–Leibler information, direct imaging and aligned SPADE scale as $\epsilon^2 s^2$ and ϵs^2 , respectively.

The singular-learning-theoretic quantities governing the local subleading asymptotics are obtained from the

zeta function associated with the Kullback–Leibler information. For each scheme $\mu \in \{\text{DI}, \text{SPADE}\}$, define

$$\zeta_{\mu}(z) := \int D_{\mu}(\epsilon, s)^z \phi(\epsilon, s) d\epsilon ds, \quad (26)$$

where $\phi(\epsilon, s)$ is a prior density that is smooth and strictly positive near $(\epsilon, s) = (0, 0)$.

After restricting the integration to a sufficiently small neighborhood of $(\epsilon, s) = (0, 0)$ and performing a smooth local rescaling, one finds at leading order

$$\zeta_{\text{DI}}(z) = \frac{C_{\text{DI}}}{(2z+1)^2}, \quad \zeta_{\text{SPADE}}(z) = \frac{C_{\text{SPADE}}}{(z+1)(2z+1)}, \quad (27)$$

for some positive constants C_{DI} and C_{SPADE} . For completeness, an explicit local zeta-integral derivation is given in Appendix E. The rightmost pole is therefore the same in both cases, namely $z = -1/2$, but the multiplicity differs:

$$(\lambda_{\text{DI}}, m_{\text{DI}}) = \left(\frac{1}{2}, 2\right), \quad (\lambda_{\text{SPADE}}, m_{\text{SPADE}}) = \left(\frac{1}{2}, 1\right). \quad (28)$$

This is the first point at which the ideal large-sample benchmark of Sec. II connects directly to singular learning theory. It is important to keep in mind, however, that the two sections concern different asymptotic regimes. The Stein exponents in Sec. II describe the limit $n \rightarrow \infty$ at fixed (ϵ, s) , whereas the singular asymptotics below describe a local regime in which (ϵ, s) approach the singular point $(0, 0)$ as n increases. The latter regime captures the finite-photon behavior near the one-source/two-source boundary, where regular asymptotics break down.

Substituting Eq. (28) into the general singular formula (21), we obtain

$$F_n^{\text{DI}} = \frac{1}{2} \log n - \log \log n + O_p(1),$$

$$F_n^{\text{SPADE}} = \frac{1}{2} \log n + O_p(1). \quad (29)$$

At this point, the distinction introduced in Sec. III becomes essential. The quantities in Eq. (29) describe singular Bayes free energies in the local prior-weighted regime; they are not, by themselves, the fixed-parameter Neyman–Pearson type-II errors of Sec. II. In particular, in the ideal aligned-SPADE setting the null distribution is supported entirely on the lowest-order mode, and as a result the usual null-side likelihood-ratio statistic has no nontrivial fluctuations. The relevant local testing quantity is therefore the Bayes-integrated local behavior induced by the same composite alternative and the same prior ϕ . Accordingly, we denote by

$$\bar{\beta}_{n,\phi}^{\mu,\text{loc}}, \quad \mu \in \{\text{DI}, \text{SPADE}\},$$

the corresponding Bayes-integrated local quantity in this aligned singular regime. With this notation, Eq. (29)

implies

$$-\frac{1}{n} \log \bar{\beta}_{n,\phi}^{\text{DI,loc}} = \frac{1}{n} \left(\frac{1}{2} \log n - \log \log n \right) + o\left(\frac{1}{n}\right), \quad (30)$$

$$-\frac{1}{n} \log \bar{\beta}_{n,\phi}^{\text{SPADE,loc}} = \frac{1}{n} \left(\frac{1}{2} \log n \right) + o\left(\frac{1}{n}\right). \quad (31)$$

The leading logarithmic term is therefore the same in both schemes, whereas direct imaging carries an additional negative $\log \log n$ correction originating from the larger multiplicity of the singularity. Thus, within the same local prior-weighted singular regime, aligned SPADE exhibits a slightly faster Bayes-integrated local decay than direct imaging. The difference appears only at the subleading logarithmic level, through the multiplicity-dependent correction. In this sense, the advantage of aligned SPADE in the present local asymptotic regime is weak but universal: the coefficients of the $\log n$ and $\log \log n$ terms are determined by the singular invariants (λ, m) , rather than by the detailed value of a fixed alternative parameter. As a numerical sanity check, we also compared the exact finite- n Bayes free energy for aligned direct imaging with the corresponding centered local asymptotic model under the same Monte Carlo samples; details are given in Appendix A. The agreement of the centered quantiles confirms that the finite- n Bayes free energy is governed by the singular asymptotic structure derived above.

B. Misaligned case: structural local scales and finite- n comparison under common physical conditions

To expose the misaligned singular structure in the simplest physically meaningful form, we study the misaligned binary-SPADE model in which one records only whether a detected photon remains in the lowest-order mode. This reduction is not introduced merely for technical convenience. In the weak-companion, sub-Rayleigh regime of interest here, the leading local effect of a faint nearby source is the leakage of probability out of the lowest-order mode. For Gaussian SPADE near ideal alignment, the total leakage out of the lowest-order mode satisfies

$$1 - P_s(0) = \frac{s^2}{4\sigma^2} + O(s^4),$$

whereas the total redistribution into modes $q \geq 2$ is only $O(s^4)$; see Appendix C. Equivalently, to leading order in s , the binary statistic $q = 0$ versus $q \geq 1$ retains the entire local $O(s^2)$ contrast, and the correction coming from the detailed higher-mode pattern enters only at order s^4 . In this sense, the binary reduction agrees with full SPADE at the level of the leading local information relevant to the present near-alignment analysis, while yield-

ing the simplest nontrivial singular testing problem induced by misalignment.

As in the previous subsection, let

$$Y_i = \begin{cases} 1, & \text{if the } i\text{th photon is detected in the mode } q = 0, \\ 0, & \text{otherwise.} \end{cases}$$

Under detector offset θ , the null hypothesis is

$$H_0 : Y_i \sim \text{Bernoulli}(p_0(\theta)), \quad (32)$$

while under the two-source alternative,

$$H_1 : Y_i \sim (1 - \epsilon) \text{Bernoulli}(p_0(\theta)) + \epsilon \text{Bernoulli}(p_s(\theta)), \quad (33)$$

with

$$p_0(\theta) = e^{-\gamma^2}, \quad p_s(\theta) = e^{-(\gamma - g_s)^2}, \quad \gamma = \frac{\theta}{2\sigma}, \quad g_s = \frac{s}{2\sigma}.$$

Thus the misaligned problem reduces to a homogeneity test for a Bernoulli mixture model, and the singular set is again given by the collapse of the alternative to the null, namely $\epsilon = 0$ or $s = 0$.

The local expansion derived in Appendix B shows that the misaligned binary-SPADE Kullback–Leibler information scales as

$$D_{\text{bSPADE}}^{\text{mis}}(\epsilon, s, \theta) \asymp \epsilon^2 s^4, \quad (34)$$

up to a nonzero θ -dependent prefactor, whereas for direct imaging one has

$$D_{\text{DI}}^{\text{mis}}(\epsilon, s, \theta) \asymp \epsilon^2 s^2. \quad (35)$$

Accordingly, the two schemes acquire nontrivial local power on different intrinsic scales:

$$\begin{aligned} s &= O(n^{-1/4}) && \text{for misaligned binary-SPADE,} \\ s &= O(n^{-1/2}) && \text{for direct imaging.} \end{aligned}$$

This intrinsic-scale statement is *structural* rather than directly operational. It identifies the local asymptotic windows in which each scheme first develops nontrivial power near the singular boundary, but it does not by itself determine which scheme performs better under a *common* physical separation s , brightness ratio ϵ , detector offset θ , and sample size n .

To make this bridge explicit, we therefore computed finite- n Neyman–Pearson powers under the same physical parameters for the two schemes. For misaligned binary-SPADE, the finite- n power can be computed *exactly* from the binomial model, using the randomized Neyman–Pearson test so that the test size is exactly α even in the discrete setting. For direct imaging, we evaluated the simple-versus-simple likelihood-ratio test by common-random-number Monte Carlo, which stabilizes the comparison across nearby values of s and n . Figure 1 summarizes the resulting finite- n comparison for the representative parameter set $\sigma = 1, \epsilon = 0.3, \theta = 0.1, \alpha = 0.05$.

Two points are immediately visible. First, on the plotted grids, direct imaging lies above the misaligned binary-SPADE curve throughout. Panels (a)–(c) of Fig. 1 show the power as a function of the physical separation s for $n = 200, 500, 2000$. In each panel the direct-imaging curve exceeds the binary-SPADE curve over the sampled range, with the gap becoming especially pronounced around $s \approx 2\theta$. Panel (d), which fixes s and varies n , shows the same tendency from a complementary viewpoint: for $s = 0.05$ and $s = 0.10$, both schemes eventually gain power with increasing n , but direct imaging rises earlier and remains higher over the plotted range.

Second, the misaligned binary-SPADE model exhibits an *exact blind separation*

$$s^* = 2\theta. \quad (36)$$

Indeed, at $s = s^*$ one has $g_s = 2\gamma$, and therefore

$$p_s(\theta)|_{s=2\theta} = \exp[-(\gamma-2\gamma)^2] = \exp(-\gamma^2) = p_0(\theta). \quad (37)$$

Hence the alternative Bernoulli parameter becomes

$$p_1 = (1 - \epsilon)p_0 + \epsilon p_{s^*} = p_0, \quad (38)$$

so that H_0 and H_1 are identical in distribution for the binary-SPADE coarse graining. Consequently, any level- α test has power exactly α at $s = s^*$. This is not a Monte Carlo artifact but an exact structural property of the misaligned binary-SPADE model. In panel (d) of

Fig. 1, this appears most clearly for $s = 0.20 = 2\theta$: the exact binary-SPADE power remains equal to α for all plotted sample sizes.

These finite- n comparisons clarify the physical meaning of the intrinsic-scale analysis. The $n^{-1/4}$ versus $n^{-1/2}$ distinction is still important, because it describes the singular local geometry of the two testing problems. However, it should not be read as implying that the misaligned binary-SPADE model enjoys a uniform practical advantage once the two schemes are evaluated under the same physical conditions. For the representative regime considered here, the opposite behavior is seen on the plotted grids: direct imaging is consistently stronger, and the binary-SPADE coarse graining suffers from the exact blind separation (36). In this sense, the ideal aligned large-sample SPADE benchmark does not directly translate into a finite- n advantage for the misaligned binary-SPADE model studied here.

V. CONCLUSION

We have analyzed far-field one-versus-two-source discrimination through the lens of singular learning theory. In the ideal aligned setting, we found that the finite-photon behavior is governed by singular invariants: direct imaging and SPADE share the same leading $\frac{1}{2} \log n$ growth, and differ only through a multiplicity-dependent subleading correction. Thus, in the local prior-weighted

singular regime considered here, aligned SPADE exhibits only a slightly faster Bayes-integrated local decay than direct imaging.

Our main physical consequence arises in the misaligned setting. There, using a misaligned binary-SPADE model motivated by the dominant local role of the lowest-order mode, we showed that direct imaging and the misaligned binary-SPADE model acquire nontrivial local power on different intrinsic sample-size scales. This intrinsic-scale distinction is structural: it identifies the local asymptotic windows in which each scheme first develops nontrivial power near the singular boundary. However, the finite- n Neyman–Pearson comparisons under common physical conditions show that, on the plotted grids, direct imaging is consistently stronger, while the misaligned binary-SPADE model exhibits an exact blind separation $s^* = 2\theta$, at which its power collapses to the significance level α . In this sense, the ideal aligned large-sample SPADE benchmark does not directly translate into a finite- n advantage for the misaligned binary-SPADE model studied here.

These results highlight model singularity as a structural feature of finite-photon quantum discrimination, rather than as a merely technical complication. Extending this viewpoint to other realistic imperfections and to broader quantum hypothesis-testing settings remains an important direction for future work.

Beyond the specific aligned and misaligned results obtained here, the broader contribution of the present work is to identify structural criteria for future receiver design in singular discrimination problems. The analysis shows that ideal aligned large-sample optimality is not, by itself, a sufficient design principle near the one-source boundary: finite- n behavior, robustness to nuisance misalignment, and the possibility of coarse-graining-induced blind separations must also be taken into account. In this sense, the present paper should be viewed less as a final prescription for practical receiver design and more as a first step toward a robustness-oriented design theory for quantum source discrimination. A natural next step is to extend the present analysis from the binary-SPADE reduction to full misaligned SPADE and to search for robust measurements or test statistics that preserve as much as possible of the aligned-SPADE advantage while avoiding structural blind spots such as the exact separation $s^* = 2\theta$ found here.

Appendix A: Numerical validation of the aligned direct-imaging asymptotics across multiple bounded prior windows

To assess how well the singular local asymptotics describe the finite- n regime, we compare under H_0 the exact finite- n Bayes free energy for aligned direct imaging with the corresponding local asymptotic approximation, after centering both quantities by the leading singular term

$$\frac{1}{2} \log n - \log \log n.$$

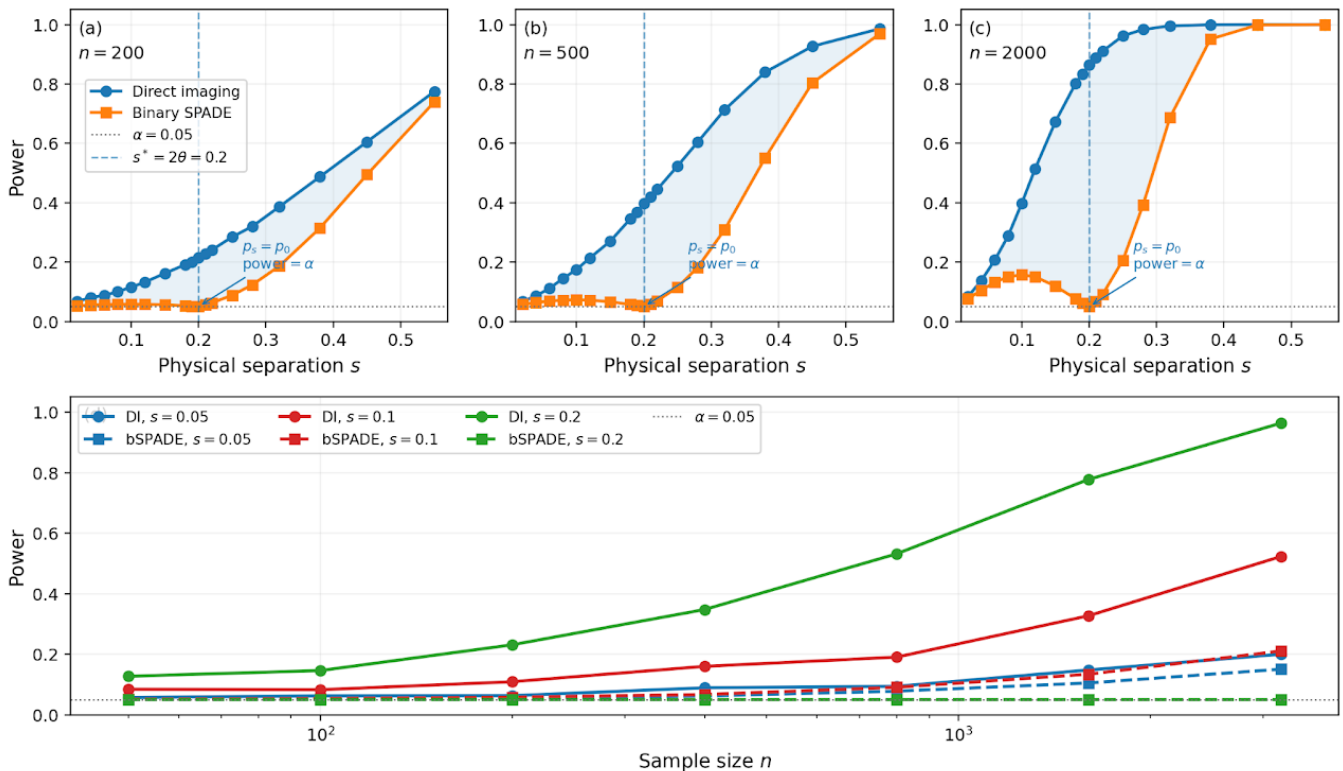


FIG. 1. Finite- n power under common physical conditions for direct imaging and the misaligned binary-SPADE model. Panels (a)–(c): power versus physical separation s for $n = 200, 500, 2000$; panel (d): power versus sample size n for fixed separations $s = 0.05, 0.10, 0.20$. Parameters are $\sigma = 1$, $\epsilon = 0.3$, $\theta = 0.1$, and $\alpha = 0.05$. For binary-SPADE, the finite- n power is computed exactly from the binomial model using the randomized Neyman–Pearson test. For direct imaging, the power is evaluated by common-random-number Monte Carlo. The dashed vertical line marks the blind separation $s^* = 2\theta = 0.2$, where $p_s(\theta) = p_0(\theta)$ exactly and the binary-SPADE power collapses to α . On the plotted grids, direct imaging remains above misaligned binary-SPADE throughout. The figure should therefore be read as a fixed-parameter finite- n comparison under common physical conditions, complementing the intrinsic-scale local asymptotic analysis given above.

More precisely, for each Monte Carlo realization we evaluate

$$\begin{aligned}\tilde{F}_n^{\text{exact}} &:= F_n^{\text{exact}} - \left(\frac{1}{2} \log n - \log \log n\right), \\ \tilde{F}_n^{\text{local}} &:= F_n^{\text{local}} - \left(\frac{1}{2} \log n - \log \log n\right),\end{aligned}$$

and compare their empirical distributions.

The purpose of this numerical check is to verify that the exact finite- n Bayes free energy is already well described, in the central part of its distribution, by the singular local model across several bounded prior windows within the weak-companion, sub-Rayleigh regime. This directly addresses the concern that the numerical agreement might be an artifact of a single ad hoc parameter choice. Accordingly, instead of fixing only one prior window, we consider three bounded uniform priors on (ϵ, s) :

$$(\epsilon_{\max}, s_{\max}/\sigma) = (0.10, 0.25), \quad (0.10, 0.30), \quad (0.15, 0.40).$$

All three windows remain in the local regime in the

sense that the leading-order direct-imaging Kullback–Leibler scale

$$D_{\max}^{\text{lead}} := \frac{\epsilon_{\max}^2 s_{\max}^2}{2\sigma^2}$$

is small throughout; the corresponding values are shown in Fig. 2. For each window and each sample size

$$n = 32, 64, 128, 256, 512, 1024, 2048,$$

we generated Monte Carlo samples under H_0 with $X_i \sim \mathcal{N}(0, \sigma^2)$ using a fixed random seed (12345).

For each realization, the exact finite- n Bayes free energy was evaluated by numerical quadrature of the bounded prior integral, while the local asymptotic approximation was evaluated from the corresponding one-dimensional local integral. In the computations shown in Fig. 2 we set $\sigma = 1$ and used Gauss–Legendre quadrature for the exact bounded-prior integral. The comparison is therefore performed under the same bounded prior window and the same Monte Carlo sample for both the exact and local quantities. Figure 2 shows, for each prior window, the empirical median and central 10%–90% quantile

band of the centered exact finite- n Bayes free energy together with those of the centered local asymptotic model. Across all three prior windows, the local model tracks the central part of the exact finite- n distribution well. As expected, the agreement is strongest for the smaller prior windows and becomes slightly less sharp as the window is enlarged, but the overall distributional structure remains stable. This is consistent with the interpretation that the exact finite- n Bayes free energy is already governed, in the relevant local regime, by the singular asymptotic structure

$$\frac{1}{2} \log n - \log \log n + O_p(1),$$

rather than by a regular large-sample approximation.

Appendix B: Derivation of the local statistics in the misaligned binary-SPADE model

In this appendix we derive the local statistics used in Sec. IV B in a form that keeps track of the misalignment-dependent prefactor before the final normalization. To make the cancellation of the linear displacement term explicit, it is convenient to parameterize the two-source configuration in local coordinates around the singular set. We therefore place the two sources at

$$x_1 = -\epsilon s, \quad x_2 = (1 - \epsilon)s,$$

with weights $1 - \epsilon$ and ϵ , respectively, so that both sources collapse to the same location as $s \rightarrow 0$.

For the $q = 0$ binary-SPADE outcome under detector offset x_D , let

$$\gamma := \frac{x_D}{2\sigma}, \quad \beta := \frac{s}{2\sigma}.$$

Under H_0 , the Bernoulli success probability is

$$p_0(\theta) = e^{-\gamma^2}. \quad (\text{B1})$$

Under H_1 , the Bernoulli success probability is

$$q_{\epsilon,s,\theta} = (1 - \epsilon) \exp[-(\gamma + \epsilon\beta)^2] + \epsilon \exp[-(\gamma - (1 - \epsilon)\beta)^2]. \quad (\text{B2})$$

Define the local shift

$$\Delta_{\epsilon,s}(\theta) := q_{\epsilon,s,\theta} - p_0(\theta). \quad (\text{B3})$$

A Taylor expansion of Eq. (B2) in β gives

$$\Delta_{\epsilon,s}(\theta) = e^{-\gamma^2} (2\gamma^2 - 1) \epsilon (1 - \epsilon) \beta^2 + O(\beta^3). \quad (\text{B4})$$

Equivalently,

$$\Delta_{\epsilon,s}(\theta) = a(\theta) u(\epsilon) s^2 + O(s^3), \quad u(\epsilon) := \epsilon(1 - \epsilon), \quad (\text{B5})$$

with

$$a(\theta) = \frac{e^{-\gamma^2} (2\gamma^2 - 1)}{4\sigma^2} = \frac{p_0(\theta) [2\gamma^2 - 1]}{4\sigma^2}. \quad (\text{B6})$$

In the small-misalignment regime considered here, $\gamma \ll 1$, so

$$e^{-\gamma^2} (2\gamma^2 - 1) = -1 + O(\gamma^2). \quad (\text{B7})$$

Hence the leading prefactor is close to -1 , and therefore

$$a(\theta) = -\frac{1}{4\sigma^2} + O(\gamma^2). \quad (\text{B8})$$

Thus, to leading order in small detector misalignment, one may regard the prefactor as a nonzero constant of order $1/\sigma^2$. Its sign is irrelevant in the final normalized local statistic, because it can be absorbed into the Gaussian fluctuation variable.

Now let $X_i \in \{0, 1\}$ denote the binary-SPADE outcome. The single-observation log-likelihood ratio is

$$\ell_i = X_i \log \frac{q_{\epsilon,s,\theta}}{p_0(\theta)} + (1 - X_i) \log \frac{1 - q_{\epsilon,s,\theta}}{1 - p_0(\theta)}. \quad (\text{B9})$$

Set $p_0 := p_0(\theta)$ and $\Delta := \Delta_{\epsilon,s}(\theta)$ for brevity. Then

$$q_{\epsilon,s,\theta} = p_0 + \Delta.$$

A second-order Taylor expansion of Eq. (B9) around $\Delta = 0$ yields

$$\ell_i = \frac{X_i - p_0}{p_0(1 - p_0)} \Delta - \frac{\Delta^2}{2p_0(1 - p_0)} + O(\Delta^3). \quad (\text{B10})$$

Summing over $i = 1, \dots, n$, we obtain

$$\sum_{i=1}^n \ell_i = \frac{\Delta}{p_0(1 - p_0)} \sum_{i=1}^n (X_i - p_0) - n \frac{\Delta^2}{2p_0(1 - p_0)} + o_p(1), \quad (\text{B11})$$

where the remainder is negligible in the local scaling used below. Introduce the null fluctuation variable

$$\xi_n := \frac{\sqrt{n}(\bar{X}_n - p_0)}{\sqrt{p_0(1 - p_0)}}, \quad \bar{X}_n := \frac{1}{n} \sum_{i=1}^n X_i. \quad (\text{B12})$$

Under H_0 , the central limit theorem gives $\xi_n \Rightarrow N(0, 1)$, and Eq. (B11) becomes

$$\sum_{i=1}^n \ell_i = \sqrt{n} \xi_n \frac{\Delta}{\sqrt{p_0(1 - p_0)}} - n \frac{\Delta^2}{2p_0(1 - p_0)} + o_p(1). \quad (\text{B13})$$

Substituting Eq. (B5) into Eq. (B13) gives

$$\begin{aligned} \sum_{i=1}^n \ell_i &= \sqrt{n} \xi_n \frac{a(\theta)}{\sqrt{p_0(1 - p_0)}} u(\epsilon) s^2 \\ &\quad - n \frac{a(\theta)^2}{2p_0(1 - p_0)} u(\epsilon)^2 s^4 + o_p(1). \end{aligned} \quad (\text{B14})$$

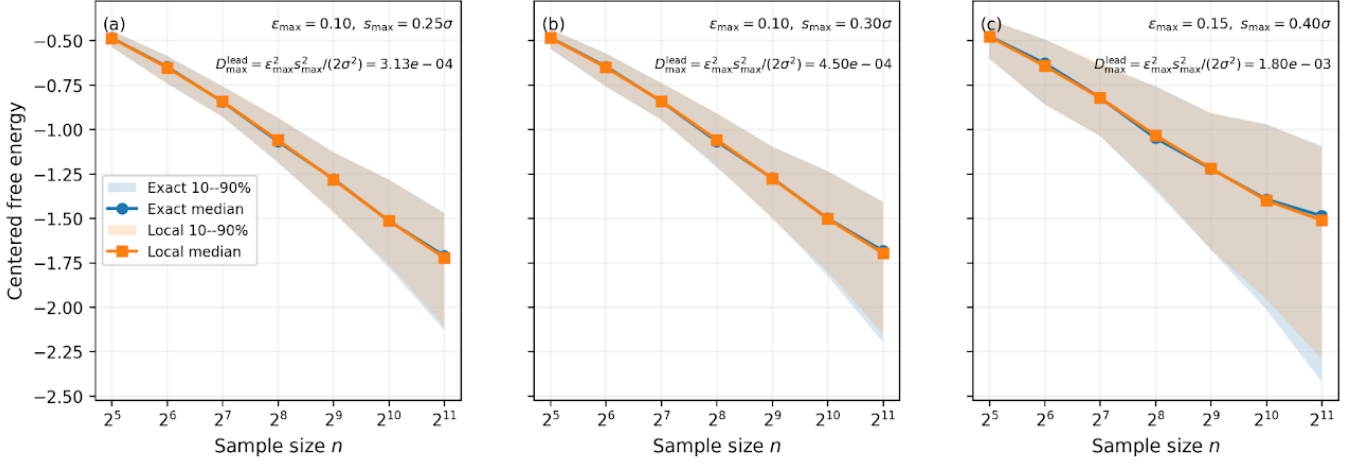


FIG. 2. Numerical validation of the aligned direct-imaging singular asymptotics across multiple bounded prior windows. For each panel, Monte Carlo samples are generated under H_0 with $X_i \sim \mathcal{N}(0, \sigma^2)$, and the centered exact finite- n Bayes free energy $\tilde{F}_n^{\text{exact}} = F_n^{\text{exact}} - (\frac{1}{2} \log n - \log \log n)$ is compared with the corresponding centered local asymptotic approximation $\tilde{F}_n^{\text{local}} = F_n^{\text{local}} - (\frac{1}{2} \log n - \log \log n)$. Solid lines show the empirical medians and shaded bands show the empirical 10%–90% quantile ranges. The three panels correspond to the bounded uniform prior windows $(\epsilon_{\max}, s_{\max}/\sigma) = (0.10, 0.25)$, $(0.10, 0.30)$, and $(0.15, 0.40)$. In each panel, $D_{\max}^{\text{lead}} = \frac{\epsilon_{\max}^2 s_{\max}^2}{2\sigma^2}$ denotes the largest leading-order direct-imaging Kullback–Leibler scale inside the corresponding prior window. The agreement across several prior windows shows that the centered finite- n Bayes free energy is already well captured, in the central part of its distribution, by the singular local model.

This confirms the generic structure quoted in the main text:

$$D_{\text{BSPADE}}^{\text{mis}}(\epsilon, s, \theta) \sim \frac{1}{2} u(\epsilon)^2 s^4,$$

up to a nonzero θ -dependent prefactor.

To normalize the coefficients, introduce the local rescaling

$$s = \left(\frac{\sqrt{p_0(1-p_0)}}{|a(\theta)|} \right)^{1/2} y n^{-1/4}, \quad 0 \leq y \leq B. \quad (\text{B15})$$

Then Eq. (B14) becomes

$$\sum_{i=1}^n \ell_i = \text{sgn}(a(\theta)) \xi_n u(\epsilon) y^2 - \frac{1}{2} u(\epsilon)^2 y^4 + o_p(1). \quad (\text{B16})$$

Since $\xi_n \Rightarrow N(0, 1)$ is symmetric, the sign of $a(\theta)$ can be absorbed into the Gaussian fluctuation variable. The Bayes factor itself involves integration over the local parameter region. Up to multiplicative factors independent of ξ_n and up to asymptotically negligible errors, the null-local statistic is therefore represented by

$$J_*^{(-)}(\xi; B) = \int_0^1 d\epsilon \int_0^B dy \exp \left[-\frac{1}{2} u(\epsilon)^2 y^4 + \xi u(\epsilon) y^2 \right], \quad (\text{B17})$$

where $\xi \sim N(0, 1)$ in the null-local limit. The omission of overall ξ -independent prefactors is harmless for test calibration, because the resulting rejection rule depends only on monotone transformations of the statistic.

It is also useful to note that $J_*^{(-)}(\xi; B)$ is strictly increasing in ξ .

Hence the critical values of the corresponding two-sided test can be calibrated directly from the standard normal quantiles of ξ .

Under the corresponding local alternative, the same expansion changes only the sign of the deterministic Kullback–Leibler contribution, so that

$$J_*^{(+)}(\xi; B) = \int_0^1 d\epsilon \int_0^B dy \exp \left[+\frac{1}{2} u(\epsilon)^2 y^4 + \xi u(\epsilon) y^2 \right]. \quad (\text{B18})$$

In this sense, the passage from $J_*^{(-)}$ to $J_*^{(+)}$ is not an ad hoc prescription, but simply reflects the sign flip of the deterministic local Kullback–Leibler contribution between the null and alternative local asymptotics. This shows explicitly how the misalignment-dependent constants are normalized away and why the local statistics take the simple forms used in Sec. IV B.

Appendix C: Why binary-SPADE captures the leading local contrast near alignment

This appendix clarifies why the binary-SPADE reduction used in Sec. IV B is physically natural in the weak-companion, sub-Rayleigh regime. For a Gaussian PSF, the SPADE mode basis is given by the Hermite–Gaussian modes adapted to the aligned source. For a source displaced by s , the corresponding mode occupation probabilities are

$$P_s(q) = |\langle \phi_q | \psi_s \rangle|^2 = e^{-\tau} \frac{\tau^q}{q!}, \quad \tau := \frac{s^2}{4\sigma^2}, \quad (\text{C1})$$

where $q = 0, 1, 2, \dots$. This can be easily seen as the $\langle \phi_q | \psi_s \rangle$ is nothing but the displaced coherent-state overlap.

In particular, for small s (equivalently small τ), the lowest-order mode probability satisfies

$$P_s(0) = e^{-\tau} = 1 - \tau + O(\tau^2), \quad (\text{C2})$$

so that the total leakage probability out of the lowest-order mode is

$$1 - P_s(0) = \tau + O(\tau^2) = \frac{s^2}{4\sigma^2} + O(s^4). \quad (\text{C3})$$

The first excited mode carries

$$P_s(1) = e^{-\tau} \tau = \tau + O(\tau^2), \quad (\text{C4})$$

whereas the total weight in all higher modes $q \geq 2$ is only

$$\sum_{q \geq 2} P_s(q) = O(\tau^2) = O(s^4). \quad (\text{C5})$$

These relations show that, near ideal alignment, the leading local effect of a small source displacement is the onset of leakage out of the lowest-order mode. The detailed redistribution among higher modes is a finer, higher-order effect. In this sense, the binary statistic

$$q = 0 \quad \text{versus} \quad q \geq 1$$

captures the dominant local contrast at order s^2 .

The misaligned analysis in Sec. IV B does not rely on the ideal aligned support structure itself; rather, it uses misalignment to turn that leading leakage channel into a nontrivial singular likelihood-ratio problem with genuine null fluctuations. The binary-SPADE reduction should therefore be understood not as an arbitrary coarse graining of the full SPADE data, but as a physically motivated minimal model that retains the leading local contrast near alignment.

Appendix D: A minimal review of singular learning theory for the present problem

For the convenience of readers unfamiliar with singular learning theory, we briefly summarize here the part of the theory that is used in the main text. We restrict attention to the quantities that enter the present one-versus-two-source discrimination problem and omit topics, such as generalization error and singular fluctuation, that are not needed below. General references include Watanabe's monograph [10] and the recent review [13]; see also Refs. [11, 12] for singular hypothesis testing in related settings.

Singular versus regular models. In a regular parametric model, the map from the parameter w to the observable probability distribution $p(\cdot | w)$ is locally one-to-one, and the Fisher information matrix is positive definite at the parameter representing the data-generating distribution. In that case, the posterior distribution is asymptotically Gaussian, and the familiar regular asymptotic theory applies. By contrast, if different parameter values yield the same observable distribution, the Fisher information degenerates and the posterior need not be Gaussian. Such a model is called *singular*. Mixture models and latent-variable models are typical examples [8–10]. The one-versus-two-source discrimination problem considered in this paper becomes singular precisely because the one-source model lies on the boundary of the two-source family.

Bayes factor, marginal likelihood, and free energy. Let $Y^n = (Y_1, \dots, Y_n)$ be independent observations, let $p_0(y)$ denote the null distribution, and let $p(y|w)$ denote the alternative model with prior density $\varphi(w)$ on a parameter space W . The marginal likelihood under the alternative is

$$m_1(Y^n) = \int_W \prod_{i=1}^n p(Y_i|w) \varphi(w) dw,$$

whereas under the null

$$m_0(Y^n) = \prod_{i=1}^n p_0(Y_i).$$

The Bayes factor is

$$\Lambda_n(Y^n) = \frac{m_1(Y^n)}{m_0(Y^n)},$$

and the minus log Bayes factor

$$F_n(Y^n) := -\log \Lambda_n(Y^n)$$

is the free-energy difference relevant for Bayesian hypothesis testing. In the present paper, this is the natural test statistic because, once the composite alternative is equipped with a prior, the null-versus-alternative problem becomes an ordinary simple-versus-simple comparison between m_0 and m_1 ; see Sec. III.

The Kullback–Leibler function and the zeta function. The asymptotic behavior of the marginal likelihood is governed by the Kullback–Leibler function

$$K(w) := \int p_0(y) \log \frac{p_0(y)}{p(y|w)} d\nu(y),$$

where ν is the underlying measure on the observation space. In regular problems, $K(w)$ has an isolated non-degenerate minimum and Laplace's method applies. In singular problems, however, the zero set

$$W_0 := \{w \in W ; K(w) = 0\}$$

typically contains singularities or higher-dimensional subsets.

A central object of singular learning theory is the zeta function

$$\zeta(z) := \int_W K(w)^z \varphi(w) dw.$$

Under the standard analyticity assumptions used in singular learning theory, $\zeta(z)$ extends meromorphically, and its poles determine the asymptotics of the marginal likelihood [10, 13].

Real log canonical threshold and multiplicity. Let $-\lambda$ be the largest pole of $\zeta(z)$ and let m be its order. Then λ is called the *real log canonical threshold* (RLCT), and m its *multiplicity*. In regular models of parameter dimension d , one has

$$\lambda = \frac{d}{2}, \quad m = 1.$$

In singular models, however, λ and m are birational invariants of the pair (K, φ) and generally differ from the regular values [10]. Intuitively, λ plays the role of an effective dimension for the leading free-energy growth, while m controls the subleading $\log \log n$ correction.

The asymptotic form of the free energy. A basic result of singular learning theory states that, in the realizable case and under suitable analyticity assumptions,

$$\begin{aligned} -\log m_1(Y^n) &= -\sum_{i=1}^n \log p_0(Y_i) + \lambda \log n \\ &\quad - (m-1) \log \log n + O_p(1). \end{aligned}$$

Hence the free-energy difference satisfies

$$F_n(Y^n) = \lambda \log n - (m-1) \log \log n + O_p(1).$$

This is the formula used in Eq. (19) of the main text. It shows that, in singular problems, the leading deterministic behavior is logarithmic in n , rather than linear in n , when the null distribution lies on the boundary of the alternative model.

Why the zeta function appears. Very briefly, the reason is as follows. A key point of resolution of singularities is that, after a suitable local change of variables, the singular structure of the Kullback–Leibler function can be reduced to a normal-crossing form. More precisely, the content relevant here is that there exist local coordinates $u = (u_1, \dots, u_d)$ such that

$$K(g(u)) = u^{2k}, \quad \varphi(g(u))|g'(u)| = |u|^h b(u),$$

with $b(u)$ positive and analytic. In other words, the theorem guarantees the existence of local coordinates in which the Kullback–Leibler function becomes monomial, or normal crossing, up to a smooth positive factor. This is the form needed to analyze both the zeta function

and the marginal likelihood asymptotically; see Atiyah’s classic treatment of this idea in the context of distributions [14], and its use in singular learning theory in Ref. [10].

Once this form is available, the local contribution to the marginal likelihood becomes an integral of monomial type, and the dominant power of n is determined by the same exponents that control the poles of $\zeta(z)$ [10, 13]. In this way, the largest pole $-\lambda$ and its order m govern the asymptotic expansion of the free energy.

In the present paper, however, the situation is simpler than in a generic singular model. For the aligned source-discrimination problem, the leading Kullback–Leibler functions are already of normal-crossing type in the original local coordinates, namely $D_{\text{DI}}(\epsilon, s) \asymp \epsilon^2 s^2$ and $D_{\text{SPADE}}(\epsilon, s) \asymp \epsilon s^2$. Therefore one does not need to carry out an additional resolution-of-singularities procedure explicitly: the zeta-function calculation can be performed directly from these local monomial forms. Resolution of singularities remains the conceptual reason that such monomial forms are the right objects to study in general, but for the present model the relevant structure is already visible without further blow-up coordinates.

Relation to the present paper. The present source-discrimination problem is singular because the one-source null model is realized inside the closure of the two-source model: for example, the alternative collapses to the null when $\epsilon = 0$ or $s = 0$. Therefore the usual regular likelihood-ratio theory is not the right asymptotic framework near the one-source boundary. Instead, the free-energy asymptotics are controlled by the singular invariants (λ, m) of the corresponding Kullback–Leibler function.

In the aligned case studied in Sec. IV A, this leads to

$$\begin{aligned} F_n^{\text{DI}} &= \frac{1}{2} \log n - \log \log n + O_p(1), \\ F_n^{\text{SPADE}} &= \frac{1}{2} \log n + O_p(1), \end{aligned}$$

because direct imaging and aligned SPADE have the same RLCT $\lambda = 1/2$ but different multiplicities $m = 2$ and $m = 1$. In the misaligned case studied in Sec. IV B, the same framework motivates the local analysis through the leading small- (ϵ, s) structure of the Kullback–Leibler function, namely

$$D_{\text{DI}}^{\text{mis}}(\epsilon, s, \theta) \asymp \epsilon^2 s^2, \quad D_{\text{bSPADE}}^{\text{mis}}(\epsilon, s, \theta) \asymp \epsilon^2 s^4.$$

These different local orders are the reason the two schemes acquire nontrivial local power on different intrinsic scales.

Appendix E: Local zeta integrals in the aligned case

For completeness, we record here the explicit local zeta-integral calculation underlying Eq. (27), and hence Eq. (28), in the aligned Gaussian case.

As explained in Sec. IV A and Appendix D, near the singular point $(\epsilon, s) = (0, 0)$ the leading Kullback–Leibler behaviors are

$$D_{\text{DI}}(\epsilon, s) \asymp \epsilon^2 s^2, \quad D_{\text{SPADE}}(\epsilon, s) \asymp \epsilon s^2, \quad (\text{E1})$$

up to smooth positive prefactors. Since the prior density $\phi(\epsilon, s)$ is assumed to be smooth and strictly positive near $(0, 0)$, it does not affect the location or multiplicity of the rightmost pole of the local zeta integral.

Accordingly, after restricting to a sufficiently small neighborhood

$$0 < \epsilon < \delta, \quad 0 < s < \delta,$$

the local zeta function for direct imaging has the same pole structure as

$$\zeta_{\text{DI}}(z) \sim \int_0^\delta d\epsilon \int_0^\delta ds (\epsilon^2 s^2)^z = \left(\int_0^\delta \epsilon^{2z} d\epsilon \right) \left(\int_0^\delta s^{2z} ds \right). \quad (\text{E2})$$

Each factor is elementary:

$$\int_0^\delta \epsilon^{2z} d\epsilon = \frac{\delta^{2z+1}}{2z+1}, \quad \int_0^\delta s^{2z} ds = \frac{\delta^{2z+1}}{2z+1}, \quad (\text{E3})$$

so that

$$\zeta_{\text{DI}}(z) \sim \frac{C_{\text{DI}}}{(2z+1)^2} \quad (\text{E4})$$

for some positive constant C_{DI} . Hence the rightmost pole is at $z = -1/2$ with multiplicity two.

For aligned SPADE, the corresponding local zeta integral has the same pole structure as

$$\zeta_{\text{SPADE}}(z) \sim \int_0^\delta d\epsilon \int_0^\delta ds (\epsilon s^2)^z = \left(\int_0^\delta \epsilon^z d\epsilon \right) \left(\int_0^\delta s^{2z} ds \right). \quad (\text{E5})$$

Now

$$\int_0^\delta \epsilon^z d\epsilon = \frac{\delta^{z+1}}{z+1}, \quad \int_0^\delta s^{2z} ds = \frac{\delta^{2z+1}}{2z+1}, \quad (\text{E6})$$

and therefore

$$\zeta_{\text{SPADE}}(z) \sim \frac{C_{\text{SPADE}}}{(z+1)(2z+1)} \quad (\text{E7})$$

for some positive constant C_{SPADE} . The rightmost pole is again at $z = -1/2$, but now with multiplicity one.

Thus,

$$(\lambda_{\text{DI}}, m_{\text{DI}}) = \left(\frac{1}{2}, 2 \right), \quad (\lambda_{\text{SPADE}}, m_{\text{SPADE}}) = \left(\frac{1}{2}, 1 \right), \quad (\text{E8})$$

which is the result quoted in Eq. (28) of the main text.

The point of this appendix is not to replace the general singular-learning-theoretic argument recalled in Appendix D, but simply to note that in the present aligned model the leading Kullback–Leibler functions are already in normal-crossing form. As a result, no additional blow-up or resolution step is needed in practice: the relevant pole structure can be read off directly from the elementary local monomial integrals above.

-
- [1] M. Tsang, R. Nair, and X.-M. Lu, *Phys. Rev. X* **6**, 031033 (2016).
[2] R. Nair and M. Tsang, *Phys. Rev. Lett.* **117**, 190801 (2016).
[3] X.-M. Lu, H. Krovi, R. Nair, S. Guha, and J. H. Shapiro, *npj Quantum Inf.* **4**, 64 (2018).
[4] M. Paúr, B. Stoklasa, Z. Hradil, L. L. Sánchez-Soto, and J. Řeháček, *Optica* **3**, 1144–1147 (2016).
[5] Z. Huang and C. Lupo, *Phys. Rev. Lett.* **127**, 130502 (2021).
[6] J. O. de Almeida, J. Kołodyński, C. Hirche, M. Lewenstein, and M. Skotiniotis, *Phys. Rev. A* **103**, 022406 (2021).
[7] J.-D. Zhang, Y. Fu, L. Hou, and S. Wang, *Opt. Express* **32**, 26147–26156 (2024).
[8] J. A. Hartigan, in *Proceedings of the Berkeley Conference in Honor of Jerzy Neyman and Jack Kiefer*, Vol. 2, pp. 807–810 (1985).
[9] J. Chen and P. Li, *Ann. Statist.* **37**, 2523–2542 (2009).
[10] S. Watanabe, *Algebraic Geometry and Statistical Learning Theory* (Cambridge University Press, Cambridge, England, 2009).
[11] N. Kariya and S. Watanabe, *Commun. Stat. Theory Methods* **51**, 5873–5888 (2022).
[12] N. Kariya and S. Watanabe, *IEICE Trans. Fundam. Electron. Commun. Comput. Sci.* **E103.A**, 1274–1282 (2020).
[13] S. Watanabe, arXiv:2406.10234 (2024).
[14] M. F. Atiyah, *Commun. Pure Appl. Math.* **13**, 145–150 (1970).
[15] K. Schlichtholz, T. Linowski, M. Walschaers, N. Treps, L. Rudnicki, and G. Sorelli, *Optica Quantum* **2**, 29–34 (2024).